Spin-orbit coupling assisted magnetoanisotropic Josephson effect in ferromagnetic graphene Josephson junctions

Chuanshuai Huang,[1,*] Yajun Wei,[1,*] Yongchun Tao,[1,†] and Jun Wang[2,‡]
[1]*Department of Physics and Institute of Theoretical Physics, Nanjing Normal University, Nanjing 210023, China*
[2]*Department of Physics, Southeast University, Nanjing 210096, China*

(Received 17 March 2020; revised 20 December 2020; accepted 4 January 2021; published 19 January 2021)

The spin-flipping effect can be induced by the Rashba spin-orbit coupling (RSOC), leading to triplet equal-spin pairs in a superconducting hybrid structure. Herein, by combining the Dirac–Bogoliubov–de Gennes equation and the Furusaki-Tsukada formalism at a finite temperature, we theoretically investigate the Josephson effect in graphene-based superconductor-ferromagnet-R-superconductor junctions, where R refers to a region with the RSOC. It is demonstrated that as a result of the RSOC, one 0-π transition can be attained by tuning the orientation of the exchange field $\vec{h}$, which is determined by its magnitude h that could be periodically taken, and the periodical 0-π transitions are also caused by manipulating h during a considerable scope of the orientation. More interestingly, although varying the RSOC strength λ cannot give rise to the 0-π transition in itself, not only is it a necessary condition for the 0-π transition induced by modulating the orientation of $\vec{h}$ but also can produce the shift of the crossover point. Furthermore, two different kinds of anomalous Josephson current effect are exhibited by controlling the orientation of $\vec{h}$. Particularly, the out-of- and in-plane magnetoanisotropic Josephson currents always exist, varying monotonically with λ while nonmonotonically with h. The characteristics may provide more insights into the proximity-induced RSOC and pave the way to a new class of tunable superconducting spintronic devices based on large-scale graphene.

DOI: 10.1103/PhysRevB.103.035418

I. INTRODUCTION

Undoped graphene is intrinsically a zero-gap semiconductor and not a superconductor (S), however, it was experimentally demonstrated that *s*-wave superconductivity could be induced in graphene via the proximity effect by depositing an S film on it [1–4]. The proximity-induced ferromagnetism in graphene has also been realized experimentally [5–9]. For the magnitude of exchange field $h > E_F$, a peculiar Andreev reflection (AR) process, a so-called specular one, is accompanied by a Klein tunneling through the exchange field *p*-*n* barrier in graphene-based ferromagnet (F)/S junctions [10]. It has been found that this spin Andreev-Klein process leads to an enhancement of the amplitude of specular AR and the resulting subgap conductance of the junctions. The corresponding Andreev-Klein bound states in graphene-based S/F/S structure are responsible for the long-range Josephson coupling [11], which shows that the Josephson current is nonvanishing at strong exchange field $h \gg E_F$. Particularly, the Josephson junction also demonstrates the existence of 0-π transitions in the structure.

Spin-orbit coupling (SOC) is central for a variety of spintronics phenomena [12,13], such as spin relaxation, spin transport, and topological quantum spin Hall effects. However, as a pure two-dimensional material, a graphene flake on a substrate lacks inversion symmetry, and it is natural to expect that Rashba spin-orbit coupling (RSOC) may introduce important changes to the material properties. Itinerant electrons in graphene have weak SOC, as they are formed primarily from p_z orbitals which have zero orbital momentum. Recently, it has experimentally been demonstrated that at an artificial interface between monolayer graphene and few-layer semiconducting tungsten disulphide (WS_2), graphene can acquire the RSOC strength λ up to 17 meV, three orders of magnitude higher than its intrinsic value [14]. The RSOC in monolayer graphene removes the spin degeneracy and creates a spin splitting 2λ at the K and K' points, but the energy splitting does not break the time-reversal symmetry, unlike the exchange splitting in the F. Thus the RSOC may affect the tunneling conductance in graphene-based R/S junctions, with R standing for the RSOC region because the RSOC mixes spin-up and spin-down states [15–17].

Vast efforts have been devoted to study the AR in the junction with the RSOC, which is composed of the F and S [18–26]. The magnetoanisotropic ARs have been recently predicted in the F/S junctions with the interfacial RSOC [22], mainly caused by unconventional AR at the F/S interface. In S/F/S junctions, the presence of interfacial RSOCs leads to the out-of-plane and in-plane magnetoanisotropies of the Josephson current [23]. In the context of the RSOC, an anomalous equal-spin AR occurs between F and S regions, where the incident electrons and the reflected holes come from the same spin subband. As a result, the spin-singlet Cooper pairs convert into the spin-triplet ones, which remarkably enhances the charge conductance or Josephson current.

*These authors contributed equally to this work.
†yctao88@163.com
‡jwang@seu.edu.cn

The spin-triplet AR is strongly dependent on the direction of magnetization, resulting in magnetoanisotropic quantum transports in the superconducting junctions. The anomalous Josephson effect has also been found in S/R/F/S heterostructures due to the breaking of time-reversal symmetry and spin rotation [25]. It has been proposed that in a graphene-based F/R/S junction, the magnitude of anomalous AR, and the triplet pairings are experimentally controllable [26]. However, in a graphene-based F/R/S junction, at the exchange field $h > E_F$, the usual or spin-triplet retro AR is replaced by a specular one, which is also determined by the direction of magnetization. Particularly, so far, the reports on the magnetoanisotropies in ferromagnetic graphene Josephson junctions remain scarce, in which similarly, the corresponding Andreev-Klein bound states are strongly sensitive to the direction of magnetization as shown in the following parts. This indicates the magnetoanisotropy of the Josephson current. It is highly desirable that the phase shift of Josephson current in such junctions could possess the 0-π transitions induced by magnetoanisotropic modulation. Especially, it is expected to maximize the control of the 0-π transition from the combination of the magnetoanisotropies and RSOC in ferromagnetic graphene Josephson junctions. Such a control can bring new functionalities into graphene-based Josephson junction devices which own low-energy dissipation and much convenience simultaneously.

In this work, therefore, we study the Josephson effect in graphene-based S/R/F/S hybrids with the ferromagnetic graphene in different exchange fields $\vec{h}$, where the triplet equal-spin pairs are induced by the RSOC. A quantum scattering method, combining the Dirac–Bogoliubov–de Gennes (DBdG) equation with the Furusaki-Tsukada formalism, is employed to calculate the Josephson current [27]. Some unique signatures of Josephson effects are exhibited due to the presence of the RSOC. We could obtain not only one 0-π transition by manipulating the orientation of exchange field $\vec{h}$ but also periodical 0-π transitions by modulating its magnitude h, where the shift of the crossover point is caused by varying the RSOC. Two different kinds of anomalous Josephson current effect are also shown by controlling the orientation of $\vec{h}$. Particularly, the out-of and in-plane magnetoanisotropic Josephson currents (MAJCs) vary monotonically with λ but nonmonotonically with h. The characteristics are ascribed to the chiral nature of the carriers in ferromagnetic graphene combined with the ferromagnetism and RSOC.

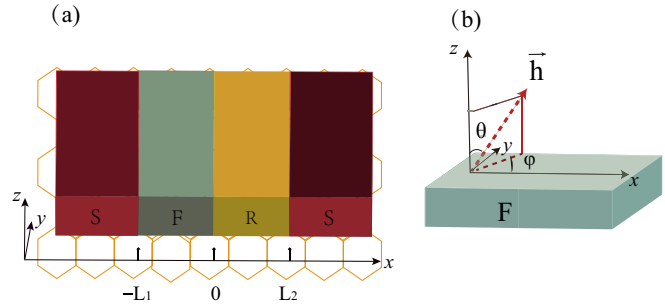

FIG. 1. (a) Schematic of the graphene-based S/F/R/S junction, with F, R, and S denoting the ferromagnetic, RSOC, and superconducting regions, respectively. (b) The orientation of $\vec{h}$ presented by the polar angle θ and azimuthal angle φ.

II. COMBINATION OF GRAPHENE-BASED MAGNETOANISOTROPIC MODULATION AND SUPERCONDUCTIVITY

Let us consider a graphene-based S/F/R/S junction as shown in Fig. 1, with the F region for $-L_1 < x < 0$, R region for $0 < x < L_2$, and two S regions for $x < -L_1$ and $x > L_2$, respectively. The low-energy excitations of the structure can be described by an extended DBdG equation [28,29], which combines the Dirac Hamiltonian with the Bogoliubov–de Gennes equation in the presence of RSOC and exchange field $\vec{h}$ as follows:

$$\begin{pmatrix} \hat{H}(x) - E_F & \Delta(x) \\ \Delta^*(x) & E_F - \hat{H}(x) \end{pmatrix} \begin{pmatrix} u \\ v \end{pmatrix} = \varepsilon \begin{pmatrix} u \\ v \end{pmatrix}, \tag{1}$$

with ε being the quasiparticles' energy relative to the Fermi energy E_F and the spinor basis in the Nambu space $(u, v)^T = [(\psi_A^{\uparrow}, \psi_B^{\uparrow}, \psi_A^{\downarrow}, \psi_B^{\downarrow})^{\tau}, (-\psi_A^{\downarrow *}, \psi_B^{\downarrow *}, \psi_A^{\uparrow *}, -\psi_B^{\uparrow *})^{\bar{\tau}}]^T$, where the index $\tau = +\ (-)$ with $\bar{\tau} = -\tau$ indicates the two so-called valleys of K (K'), the arrow index $(\uparrow, \downarrow)$ corresponds to real spin, and A and B denote the two trigonal sublattices. The single-particle Hamiltonian is given by

$$\hat{H}(x) = H_0 + \begin{cases} H_F = -\sigma_0 \otimes \vec{h} \cdot \vec{\sigma}, & -L_1 < x < 0, \\ H_{RSOC} = \lambda(s_y \otimes \sigma_x - \tau s_x \otimes \sigma_y), & 0 < x < L_2, \\ H_S = -U_0 s_0 \otimes \sigma_0, & x > L_2, x < -L_1, \end{cases} \tag{2}$$

with a two-dimensional Dirac Hamiltonian of a linear dispersion at low energies $H_0 = \hbar v_F s_0 \otimes (\sigma_x k_x + \tau \sigma_y k_y)$, where k_x and k_y are respectively the components of wave vectors in the x and y directions, σ_i $(i = 1, 2, 3)$ and s_i represent the Pauli matrices acting on the pseudospin and real-spin degrees of freedom, respectively, both σ_0 and s_0 stand for the 2×2 identity matrix, and v_F means the Fermi velocity in graphene. The exchange field $\vec{h}$ is given by $h(\sin\theta\cos\varphi, \sin\theta\sin\varphi, \cos\theta)$ with the polar angle θ and the azimuthal angle φ. λ and U_0 are the RSOC strength and electrostatic potential in the two superconducting regions, respectively. Neglecting the proximity effect in the F/S interface, the superconducting pairing potential is given by $\Delta(x) = \Delta(T)[\Theta(-x - L_1)e^{i\phi_L} + \Theta(x - L_2)e^{i\phi_R}]$, with $\Delta(T) = \Delta_0 \tanh(1.74\sqrt{T_c/T - 1})$ and $\phi_{L(R)}$ the macroscopic phase of the left (right) S.

Due to the valley degeneracy, we consider $\hat{H}(x)$ only including the K valley with τ_+ in Eq. (1). By solving the DBdG equation, we can obtain the states of electronic and

hole excitations in each region, which are described by the eigenfunctions. With an incident spin-up electronlike quasiparticle (ELQ) from the left S at an angle α with energy ε, the total wave functions in the different regions can be constructed from the linear combination of corresponding electronlike and holelike states. We assume that the junction width W is enough large so that the y component of the wave vector k_y is a conserved quantity upon the scattering. The total wave function in the left S region is given by

$$\Psi_L^S(x) = \Psi_{e,1}^{S+} + r_1\Psi_{e,1}^{S-} + r_2\Psi_{e,2}^{S-} + r_{A1}\Psi_{h,1}^{S-} + r_{A2}\Psi_{h,2}^{S-} \tag{3}$$

for $x < -L_1$, where

$$\psi_{e,1}^{S\pm}(x) = (e^{+i\beta}, \pm e^{+i\beta\pm i\gamma}, 0^2, e^{-i\phi}, \pm e^{-i\phi\pm i\gamma}, 0^2)^T e^{\pm k_x^{S,e}x}, \quad \psi_{e,2}^{S\pm}(x) = (0^2, e^{+i\beta}, \pm e^{+i\beta\pm i\gamma}, 0^2, e^{-i\phi}, \pm e^{-i\phi\pm i\gamma})^T e^{\pm k_x^{S,e}x},$$
$$\psi_{h,1}^{S\pm}(x) = (e^{-i\beta}, \mp e^{-i\beta\mp i\gamma}, 0^2, e^{-i\phi}, \mp e^{-i\phi\mp i\gamma}, 0^2)^T e^{\mp k_x^{S,h}x}, \quad \psi_{h,2}^{S\pm}(x) = (0^2, e^{-i\beta}, \mp e^{-i\beta\mp i\gamma}, 0^2, e^{-i\phi}, \mp e^{-i\phi\mp i\gamma})^T e^{\mp k_x^{S,h}x}, \tag{4}$$

with $\beta = \arccos(\varepsilon/\Delta_0)$, $\gamma = \arcsin[\hbar v_F k_y/(U_0 + E_F)]$, $k_x^{S,e} = (E_F + U_0 + \Omega)/(\hbar v_F)$, $k_x^{S,h} = (E_F + U_0 - \Omega)/(\hbar v_F)$, $\Omega = \sqrt{\varepsilon^2 - \Delta_0^2}$, with 0^n representing a $1\times n$ matrix with only zero entries, and T being a transpose operator. The scattering coefficients $r_{1(2)}$ and $r_{A1(2)}$ are respectively corresponding to the normal reflection without (with) a spin flip and the usual (novel) AR. In the F region, we have the wave function

$$\Psi^F(x) = a_1\Psi_{e,\uparrow}^{F+}(x) + a_2\Psi_{e,\uparrow}^{F-}(x) + a_3\Psi_{e,\downarrow}^{F+}(x) + a_4\Psi_{e,\downarrow}^{F-}(x) + a_5\Psi_{h,\uparrow}^{F+}(x) + a_6\Psi_{h,\uparrow}^{F-}(x) + a_7\Psi_{h,\downarrow}^{F+}(x) + a_8\Psi_{h,\downarrow}^{F-}(x) \tag{5}$$

for $-L_1 < x < 0$, where

$$\psi_{e\uparrow}^{F\pm}(x) = \left(\cos\frac{\theta}{2}e^{-i\varphi}, \pm\cos\frac{\theta}{2}e^{-i\varphi}e^{\pm i\alpha_\uparrow^e}, \sin\frac{\theta}{2}, \pm\sin\frac{\theta}{2}e^{\pm i\alpha_\uparrow^e}, 0^4\right)^T e^{\pm ik_{x\uparrow}^{F,e}x},$$
$$\psi_{e\downarrow}^{F\pm}(x) = \left(-\sin\frac{\theta}{2}e^{-i\varphi}, \mp\sin\frac{\theta}{2}e^{-i\varphi}e^{\pm i\alpha_\downarrow^e}, \cos\frac{\theta}{2}, \pm\cos\frac{\theta}{2}e^{\pm i\alpha_\downarrow^e}, 0^4\right)^T e^{\pm ik_{x\downarrow}^{F,e}x},$$
$$\psi_{h\uparrow}^{F\pm}(x) = \left(0^4, -\sin\frac{\theta}{2}, \pm\sin\frac{\theta}{2}e^{\pm i\alpha_\uparrow^h}, \cos\frac{\theta}{2}e^{-i\varphi}, \mp\cos\frac{\theta}{2}e^{-i\varphi}e^{\pm i\alpha_\uparrow^h}\right)^T e^{\pm ik_{x\uparrow}^{F,h}x},$$
$$\psi_{h\downarrow}^{F\pm}(x) = \left(0^4, \cos\frac{\theta}{2}, \mp\cos\frac{\theta}{2}e^{\pm i\alpha_\downarrow^h}, \sin\frac{\theta}{2}e^{-i\varphi}, \mp\sin\frac{\theta}{2}e^{-i\varphi}e^{\pm i\alpha_\downarrow^h}\right)^T e^{\pm ik_{x\downarrow}^{F,h}x}. \tag{6}$$

The propagation angles are given by $\alpha_{\uparrow\downarrow}^{e(h)} = \arcsin[\hbar v_F k_y/(\varepsilon + (-)E_F + \sigma h)]$. The x component of wave vectors during the scattering processes can be accordingly expressed by

$$k_{x\uparrow}^{F,e} = (\varepsilon + E_F + h)\cos\alpha_\uparrow^e/(\hbar v_F),$$
$$k_{x\downarrow}^{F,e} = (\varepsilon + E_F - h)\cos\alpha_\downarrow^e/(\hbar v_F),$$
$$k_{x\uparrow}^{F,h} = (\varepsilon - E_F - h)\cos\alpha_\uparrow^h/(\hbar v_F),$$
$$k_{x\downarrow}^{F,h} = (\varepsilon - E_F + h)\cos\alpha_\downarrow^h/(\hbar v_F). \tag{7}$$

The wave function in the R region is given by

$$\Psi^R(x) = b_1\Psi_{e,+}^{R+}(x) + b_2\Psi_{e,-}^{R-}(x) + b_3\Psi_{e,+}^{R-}(x) + b_4\Psi_{e,-}^{R+}(x) + b_5\Psi_{h,+}^{R+}(x) + b_6\Psi_{h,-}^{R-}(x) + b_7\Psi_{h,+}^{R-}(x) + b_8\Psi_{h,-}^{R+}(x) \tag{8}$$

for $0 < x < L_2$, where

$$\psi_{e,\eta=+1}^{R\pm}(x) = (\mp if_+^e e^{\mp i\theta_+^e}, -i, 1, \pm f_+^e e^{\pm i\theta_+^e}, 0^4)^T e^{\pm ik_{x,+}^{R,e}x},$$
$$\psi_{e,\eta=-1}^{R\pm}(x) = (\pm f_-^e e^{\mp i\theta_-^e}, 1, -i, \mp if_-^e e^{\pm i\theta_-^e}, 0^4)^T e^{\pm ik_{x,-}^{R,e}x},$$
$$\psi_{h,\eta=+1}^{R\pm}(x) = (0^4, \mp if_+^h e^{\mp i\theta_+^h}, -i, 1, \pm f_+^h e^{\pm i\theta_+^e})^T e^{\pm ik_{x,+}^{R,h}x},$$
$$\psi_{h,\eta=-1}^{R\pm}(x) = (0^4, \pm f_-^h e^{\mp i\theta_-^h}, 1, -i, \mp if_-^h e^{\pm i\theta_-^e})^T e^{\pm ik_{x,-}^{R,h}x}. \tag{9}$$

Accordingly, the x component of wave vectors during the scattering processes can be expressed by $k_{x,\eta}^{R,e} = (E_F + \varepsilon)f_\eta^e\cos\theta_\eta^e/(\hbar v_F)$, $k_{x,\eta}^{R,h} = (E_F - \varepsilon)f_\eta^h\cos\theta_\eta^h/(\hbar v_F)$, and the definition of auxiliary parameters are $f_\eta^e = \sqrt{1 + 2\eta\lambda(E_F + \varepsilon)^{-1}}$, $f_\eta^h = \sqrt{1 + 2\eta\lambda(E_F - \varepsilon)^{-1}}$, where $\theta_\eta^{e(h)}$ are the electron and hole propagation angles, respectively. The wave function in the right S region is given by

$$\Psi_R^S(x) = t_1\Psi_{e,1}^{s+}(x) + t_2\Psi_{e,2}^{s+}(x) + t_3\Psi_{h,1}^{s+}(x) + t_4\Psi_{h,2}^{s+}(x) \tag{10}$$

for $x > L_2$, where $t_{1(2)}$ and $t_{3(4)}$ are the usual (novel) transmission as ELQs and the usual (novel) transmission as holelike quasiparticles (HLQs), respectively.

All the coefficients will be determined by matching the boundary conditions

$$\Psi_L^S(x)|_{x=-L_{1-}} = \Psi^F(x)|_{x=-L_{1+}},$$
$$\Psi^F(x)|_{x=0_-} = \Psi^R(x)_{x=0_+},$$
$$\Psi^R(x)_{x=L_{2-}} = \Psi_R^S(x)_{x=L_{2+}}. \tag{11}$$

Analogously, one can easily obtain r_{A1} and r_{A2} for the incident spin-down ELQ, and then the scattering coefficients of the ARs r_{A3} and r_{A4} for the incident spin-σ HLQ with energy $\varepsilon > \Delta$ from the left S region. The analytical expressions for

r_{Ai} $(i = 1, 2, 3, 4)$ are extremely tedious and thus not given here.

The dc Josephson current at a given temperature can be expressed in terms of r_{Ai} by using the temperature Green's function formalism, the Furusaki-Tsukada formalism [27]

$$I(\phi) = \frac{e\Delta}{2\hbar} \sum_{\sigma,k_y} k_B T \sum_{\omega_n} \frac{1}{2\Omega_n}\left(k_n^e + k_n^h\right) \times \left(\frac{r_{An}^1 + r_{An}^2}{k_n^e} - \frac{r_{An}^3 + r_{An}^4}{k_n^h}\right), \tag{12}$$

where $k_n^e, k_n^h, r_{An}^1, r_{An}^2, r_{An}^3, r_{An}^4$ are obtained from k_e^S, k_h^S, r_{A1}, r_{A2}, r_{A3}, r_{A4} by the analytic continuation $\varepsilon \to i\omega_n$, the Matsubara frequencies are $\omega_n = \pi k_B T(2n+1)$ with $n = 0, \pm1, \pm2, \ldots$, $\Omega_n = \sqrt{\omega_n^2 + \Delta^2}$, and $\phi = \phi_R - \phi_L$ is the macroscopic phase difference across the junction.

In the calculations, the normalizations of the Josephson current, energies, and lengths are respectively by $R = 2\hbar^2\pi\upsilon_F/(e^2 W E_F)$, Δ_0, and the superconducting coherent length $\xi = \hbar v_F/\Delta_0$ for simplicity. We set the low temperature $T = 0.1T_c$ with the critical temperature $T_c = 0.57\Delta_0/k_B$ based on BCS theory and Fermi energy $E_F = 15\Delta_0$ for the weakly doped situation in the F region. $\Delta_0 \ll E_F + U_0$ is assumed for the mean-field requirement of superconductivity, i.e., the Fermi wave vector in the S region should be much larger than that in the F one [30].

In terms of realistic parameters, we choose the typical superconducting energy gap $\Delta_0 = 1$ meV and the coherence length $\xi = 10$ nm if the S is Nb [31]. It was demonstrated that the graphene interfacing with WS_2 could acquire the RSOC strength λ up to 17 meV because of the proximity effect [14], which means that λ can be taken $0 - 17\Delta_0$. According to the first-principles calculations, the RSOC in graphene can be induced by the transverse electric field E. It creates a spin-splitting 2λ at K or K' points that has a linear dependence on E, about 50 μeV per V/Å for the zero-buckling case [32,33]. Note that the former stems from the proximity effect while the latter from $\sigma - \pi$ mixing. Furthermore, it is shown that EuS could induce a large magnetic exchange field (>14 tesla) in graphene with the potential to reach hundreds of tesla [5], and thus we assume that the magnetization strength $h > 10$ meV can be realized in the experiments. Moreover, the Fermi energy E_F in graphene is usually in the order of $0 - 100$ meV [34] and can be shifted in a controllable fashion (by doping or electric fields).

III. RESULTS AND DISCUSSION

A. Two kinds of current-phase relations

On the basis of Eq. (12), we calculate the Josephson current as a function of ϕ for different polar angle θ, the current-phase relation $I(\phi)$, as shown in Fig. 2, where the azimuthal angle $\varphi = 0$ is fixed and the polar angle θ is varied in the $x - z$ plane. It is found that the effect of θ on $I(\phi)$ is strongly determined by the exchange field magnitude h and the deviation from the sine function is always exhibited. In Fig. 2(a) for $h = 4\Delta_0$, the 0-π transition tuned by the orientation of $\vec{h}$ is shown. At $\theta = 0$, the junction is in the stable π state. With increasing θ, the coexistence of 0 and π states emerges. When θ is enhanced to 0.15π, the 0-π transition takes place. With θ increased from 0.3π up to 0.5π, the junction remains the stable 0 state throughout and its corresponding curves of $I(\phi)$ approach the sine function. However, the characteristics shown in Fig. 2(b) for $h = 15\Delta_0$ are thoroughly different from those in Fig. 2(a). For θ from 0 up to 0.5π, the curves all approach the sine function, particularly, the junction keeps the stable 0 state all the time, accompanied by the increase of the current with θ except for at $\phi = 0$ and π. These indicate that whether the 0-π transition exists or not is determined by the initial state. It follows that the characteristics of magnetoanisotropic modulation are strongly dependent on the exchange field h, which determines not only the initial state but also if the 0-π transition can be induced by magnetoanisotropic modulation or not. The characteristics can be explained by the Andreev bound states (ABSs) in the following, carrying the Josephson currents.

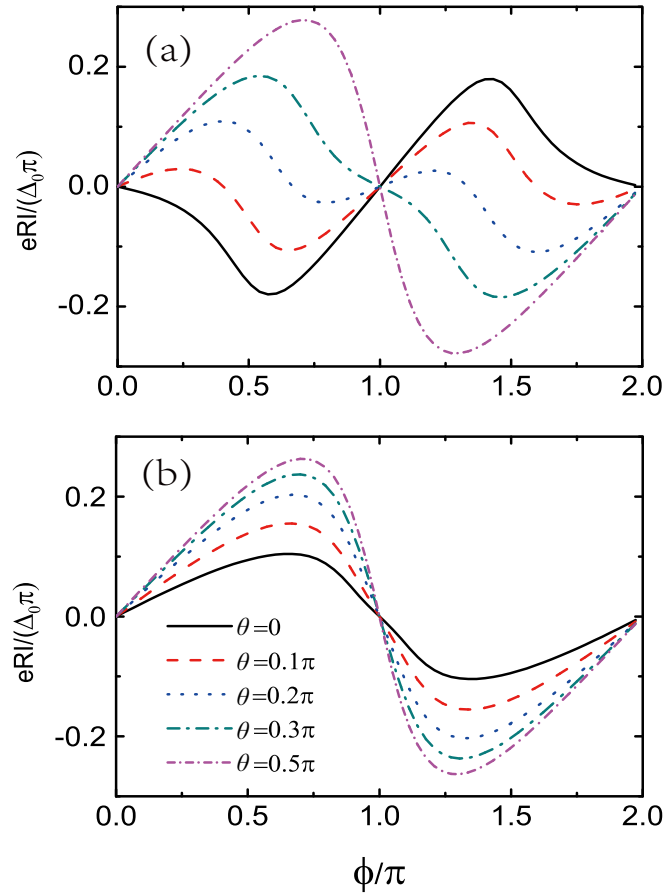

FIG. 2. The current-phase relation $I(\phi)$ at different θ in the x-z plane ($\varphi = 0$), where $E_F = 15\Delta_0$, $L_1 = 0.2\xi$, $L_2 = 0.1\xi$, $\lambda = 4\Delta_0$, $h = 4\Delta_0$ (a) and $15\Delta_0$ (b).

B. Anomalous Josephson current effect

The current-phase relations $I(\phi)$ for different polar angles θ in the y-z plane ($\varphi = -\pi/2$) and different azimuthal angle φ in the x-y plane ($\theta = \pi/2$) are shown in Figs. 3(a) and 3(b), respectively. For the former, the sine function landscape can be found to basically remain, and with increasing θ, $I(\phi)$ at $\phi < 0.3\pi$ is enhanced while it is suppressed in the range of 0.3π to π. Particularly, at $\theta \neq 0$, the Josephson current

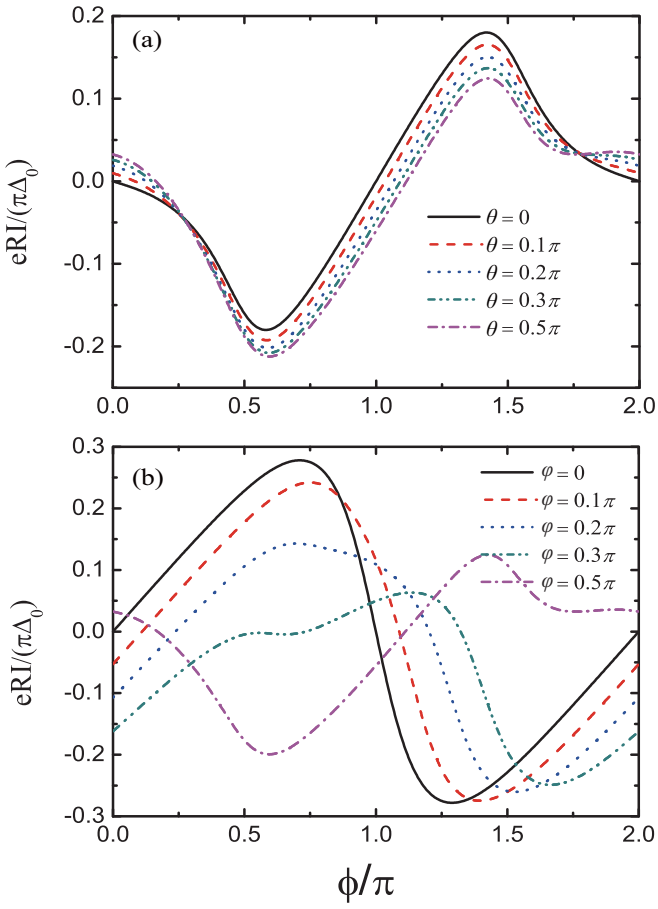

FIG. 3. $I(\phi)$ (a) for different θ in the y-z plane ($\varphi = -\pi/2$) and (b) for different φ in the x-y plane ($\theta = \pi/2$), where $h = 4\Delta_0$ and the other parameters are the same as those in Fig. 2.

$I(\phi = 0)$ is no longer zero and increased with θ, indicating the so-called anomalous Josephson effect. However, for the latter, with the enhancement of φ, the obvious deviation from the sine function always displays. Especially, the anomalous Josephson effect also takes up, and with increasing φ, the corresponding $I(\phi = 0)$ could be not only negative but also positive. The anomalous Josephson effect will not be specifically discussed in this work.

C. Magnetoanisotropic dependence of Andreev bound energies

The ABS spectrum can be obtained numerically. The boundary conditions, Eq. (11), can be organized neatly into a matrix equation of the form $Az = 0$, where the 24×24 matrix A is a function of ε, ϕ, and k_y, and z is a column vector containing 24 unknown coefficients. A nontrivial solution requires the determinant of matrix A, $\det A = 0$, from which the ABSs can be obtained in the form of a relation between ε and ϕ at a given k_y, i.e., the dispersion $\varepsilon_i(\phi)$ ($i = 1, \ldots, 4$) due to the coherent subgap processes [35], corresponding to $\pm\varepsilon_\sigma$. Without loss of generality, we only give the results for the case of the vertical incidence ($k_y = 0$) and neglect the difference of the wave vectors of ELQ and HLQ.

The typical energy-phase relation for ABSs in the S/normal metal/S junction is obtained as [36,37] $\varepsilon_{n\sigma} = \pm\Delta\sqrt{1 - D_n \sin^2(\phi/2)}$, where the junction is characterized by a set of transport channels labeled $n = 0, 1, \ldots, N$ and the transmission coefficient D_n is determined by the transverse momentum k_y. In the ballistic regime ($D_n = 1$ with $k_y = 0$), there exist two levels, one with the positive sign in $\varepsilon_{n\sigma}$ is corresponding to the left-moving electrons, the other with the negative one corresponds to the right-moving electrons, cross at $\phi = \pi$. The gap opens for $D_n < 1$ with $k_y \neq 0$. In an S/F/S junction, the different phase shifts for different spin directions result in a spin-dependent energy shift of the ABSs, and two zero-energy Andreev levels are located at the phase differences $\pi + \delta\phi$ with $\delta\phi$ dependent of the value of $k^\sigma_{\varepsilon=0}L_1$.

For the usual F/S junction, the AR occurs at the interface, in which the incident spin-up electron from the F region is reflected back as a spin-down hole and thus a Cooper pair is injected into the S. The opposite-spin AR and the resultant corresponding ABSs are strongly affected by the spin polarization of the F lead [38]. However, in the presence of interfacial RSOC, which breaks the inversion symmetry of the lattice, triplet equal-spin AR or equal-spin pairs can be induced in the F with the incident electrons and the reflected holes coming from the same spin subband. As for the present graphene-based S/F/R/S junction, the spin-dependent AR occurs at the right interface, and a right-moving spin-up electron is reflected as a left-moving hole that has both spin-up and -down components due to the RSOC region. The phase dependences of the ABS ε_σ for the junction are illustrated in Fig. 4, where Figs. 4(a)–4(c) and Figs. 4(d)–4(f) are respectively corresponding to Figs. 2(a) and 2(b). The spin directions have been denoted in the phase-dependent spectrum [see Fig. 4(b)]. It is found that for the small h, with the increase of θ, the spin splitting first strengthens, then weakens, and finally the energy band becomes degenerate at $\theta = 0.5\pi$, while for the large h, the spin splitting monotonically weakens. The degeneration at $\theta = 0.5\pi$ corresponds to the vanished opposite-spin AR with the reflected holes all coming from the same spin band as the incident electrons. An extra momentum change $2h/v_F$ and a resultant phase shift induced in the opposite-spin AR [39], leading to the so-called π junction, could not be exhibited in the equal-spin AR. This means that the junction at $\theta = 0.5\pi$ is always in the stable 0 state.

Now we investigate the relation of the spins close to zero-energy states and the 0-π transition. For $\varepsilon > 0$, except for θ near 0.5π, the spin-up and -down bound energy levels are all taken far apart for other θ, as shown in Figs. 4(a), 4(b), 4(d), and 4(e), and only the spin-down one owes the zero-energy states, implying the spins close to zero-energy states are spin down. However, at θ approaching 0.5π, the two kinds of levels are dragged very closely, therefore although only the spin-down level has the zero-energy states, and the spins near them are partially spin up. Obviously, due to degeneration of the spin-up and -down levels at $\theta = 0.5\pi$, the proportions of up and down spins at the neighborhood of zero-energy states are evenly distributed [see Figs. 4(c) and 4(f)]. The same behaviors for $\varepsilon < 0$ can be exhibited. As a result, the change of spin close to the zero-energy state does not indicate a conversion of different states (0-π state transition). This is much different from that for the S with magnetic impurities as deduced by Sakurai in Ref. [40]. In the S, there exist two kinds of states: one is the so-called state ψ, closely connected with the continuum and bound modes, the other is the one ψ'

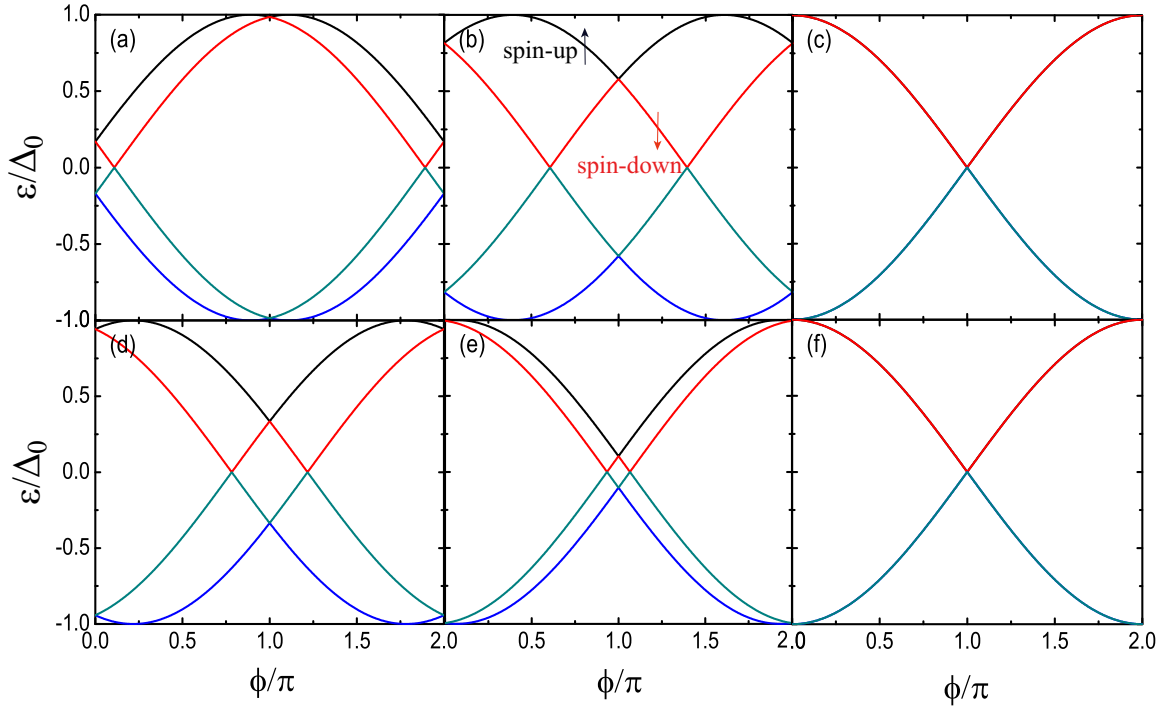

FIG. 4. Spin-splitting dispersion of ABS $\pm\varepsilon_\sigma$ for different h and θ of $\vec{h}$ in the x-z plane ($\varphi = 0$) at the incident angle $\alpha = 0$. Here, $\theta = 0$ for (a) and (d), $\theta = 0.2\pi$ for (b) and (e), $\theta = 0.5\pi$ for (c) and (f), $h = 4\Delta_0$ for the top row, and $15\Delta_0$ for the bottom row, and the other parameters are the same as those in Fig. 2.

only determined by the continuum mode. One bound mode β_0 can localize a half spin-up electron and the continuum one camps a spin-down electron. With the interaction strength ζ increasing, the total spin density at the impurity site in the state ψ decreases from 0 and approaches -1 and ψ turns into the lowest excited state from the ground one at $\zeta = 1$. However, ψ' is the lowest excited one for weak interactions while becoming the ground one for $\zeta > 1$. The ground state abruptly changes to ψ' from ψ at $\zeta = 1$. It follows that the interchange of different states is accompanied with the change of the total spin density at the impurity site.

Either the 0 or π state can be seen from the free energy, which depends on the ABS, as shown in Fig. 5. The 0 or π state for the Josephson junction is determined by the minimum of the ϕ-dependent free energy [41],

$$F(\phi) = -\frac{1}{\beta}\ln[\prod_i (1 + e^{-\beta\varepsilon_i(\phi)})] = -\frac{1}{\beta}\sum_\sigma \ln\left[2\cosh\left(\frac{\beta\varepsilon_\sigma(\phi)}{2}\right)\right]. \quad (13)$$

The corresponding $F(\phi)$ for the same three directions of $\vec{h}$ as in Fig. 4(a)–4(c), respectively, are shown in Fig. 5(a), where the curves of $F(\phi)$ are found to be all symmetrical about the axis $\phi = \pi$. When $\theta = 0$ with the orientation of $\vec{h}$ normal to the x-y plane, the maximum and minimum are located at $\phi = 0\ (2\pi)$ and π, respectively. With θ increased, the locations of the two maximums gradually approach the axis $\phi = \pi$, while the two minimums start to be at $\phi = 0$ and 2π from some polar angle θ, respectively, indicating a 0-π transition. As θ is increased to $\pi/2$, i.e., the orientation of $\vec{h}$ lies in the x-y plane, the maximum exhibits at the axis $\phi = \pi$, whereas the minimum is located at $\phi = 0\ (2\pi)$, which means the structure is in the stable 0 state. Figure 5(b) shows $F(\phi)$ corresponding to Figs. 4(d)–4(f). However, the two minimums for different

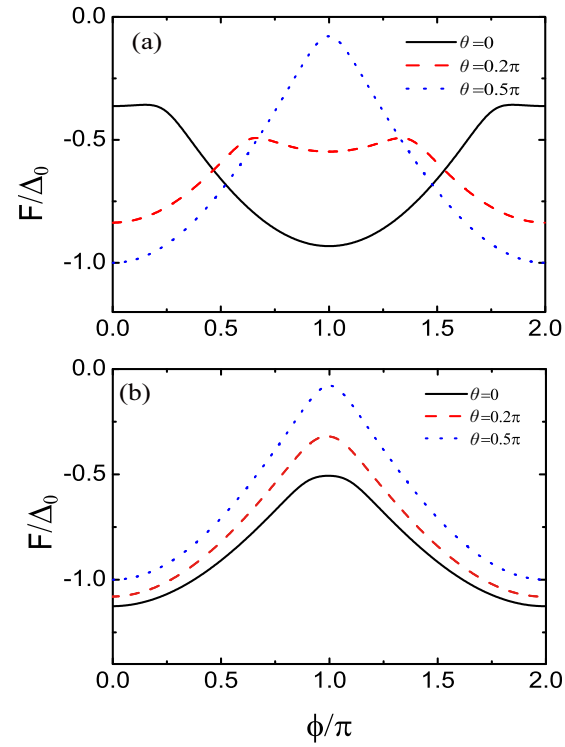

FIG. 5. Free energy $F(\phi)$ for different θ in the x-z plane ($\varphi = 0$), where (a) $h = 4\Delta_0$, (b) $h = 15\Delta_0$, and the other parameters are the same as those in Fig. 2.

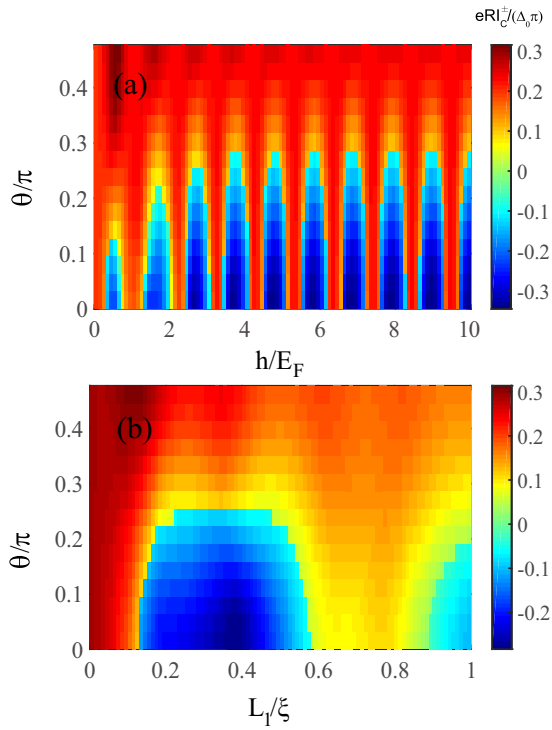

FIG. 6. The critical supercurrent $I_c^{\pm}$ (a) as a function of θ and h at $L_1 = 0.2\xi$ and (b) a function of θ and L_1 at $h = 4\Delta_0$, where the other parameters are unchanged.

θ are always located at $\phi = 0$ and 2π, respectively, which means that the junction is in the stable 0 state all the way.

D. Two different phases of the critical Josephson current

In order to get a much more in-depth look at the θ dependence of the Josephson current, we now turn to the critical Josephson current. It is defined as $I_c = \max|I(\phi)|$ and further divided into $I_c^{\pm} = \pm\max|I(\phi)|$ with the positive and negative signs corresponding to the 0 and π states, respectively, the experimentally measured relevant quantities. The Josephson current can be also estimated by the ABSs [35,42]:

$$I(\phi) = \frac{2e}{\hbar}\sum_i f(\varepsilon_i)\frac{d\varepsilon_i}{d\phi} = -\frac{2e}{\hbar}\sum_\sigma \tanh\left(\frac{\beta\varepsilon_\sigma}{2}\right)\frac{d\varepsilon_\sigma}{d\phi}. \quad (14)$$

The phase shift induced by the extra momentum change $2h/v_F$ of the reflected hole due to the F region, in the context of dimensionless units, is approximately $\eta = (k_- - k_+)L_1 \sim hL_1$ as in Ref. [43]. However, in the presence of RSOC, the phase shift is determined by not only hL_1 but also the orientation of $\vec{h}$ and RSOC strength λ.

The dependences of $I_c^{\pm}$ on θ and h are shown in Fig. 6(a). With h increased, two different parts or phases are exhibited. One is that for larger θ, there only exists the 0 state, and the other is that for smaller θ, the 0 and π states emerge alternately, indicating that the 0-π transition appears periodically with increasing h; however, both of the initial states are always the stable 0 ones regardless of θ. And with the enhancement of θ, there exist two kinds of phases with and without one 0-π transition, respectively, which appear alternately with the variation of h. Which phase emerges with increasing θ is determined by the initial state, and it must be only the π one for the former. As shown in Fig. 2, the initial state is strongly dependent on h. More interestingly, in the first three phases with the $0-\pi$ transition, θ corresponding to the crossover point gradually increases while remaining almost unchanged in the subsequent ones. As λ is other values, the characteristics including the period of h are found to remain the same, except for the different magnitudes of $I_c^{\pm}$, which are not presented by the figures for simplicity.

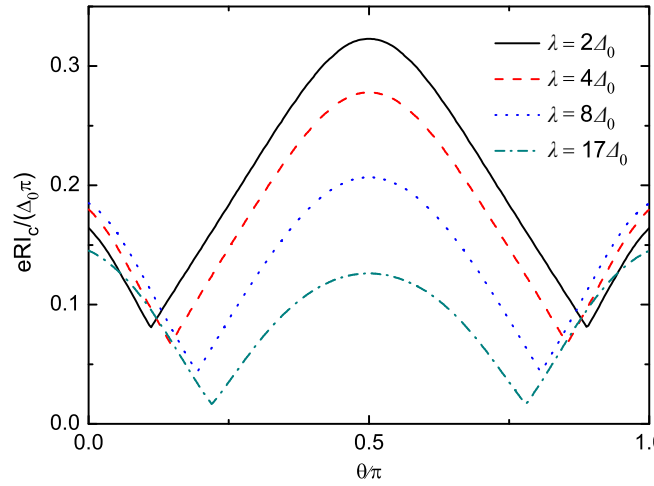

FIG. 7. I_c as a function of θ for $h = 4\Delta_0$ with the other parameters unchanged.

In Fig. 6(b), $I_c^{\pm}$ as a function of θ and the F region length L_1 are also illustrated, where similar characteristics with those in Fig. 6(a) are displayed. Although the 0-π transition appears periodically with increasing L_1, the $I_c^{\pm}$ display the trend of gradual decay, which is much different from that in Fig. 6(a).

Unlike the ferromagnetism of the F layer in the s-wave S/F/S junction, the RSOC of the R layer cannot reverse the supercurrent or give rise to the 0-π transition in the s-wave S/R/S junction [44–46] because the RSOC maintains time-reversal symmetry, leading to the result that the singlet Cooper pair cannot achieve any extra phase shift π after entering into the R region. In the present graphene-based S/F/R/S hybrid structure, the spin-flipping effect induced by RSOC generates the triplet equal-spin pairs but cannot achieve any phase shift for $I(\phi)$ as well, as mentioned in Sec. III C, so that the RSOC could not induce the 0-π transition. However, it has an influence on the crossover point of the 0-π transition as shown in Fig. 7. The dependences of the critical current I_c on θ for different λ are shown in Fig. 7. It is clearly seen that the curves are symmetric about the axis $\theta = \pi/2$, and with increasing λ, the values of the peak and two dips (crossover points of 0-π transition) are all decreased, in particular, the two crossover points shift towards the axis $\theta = \pi/2$.

E. MAJC

Although the RSOC is characterized by spin-triplet pairs in the present hybrid structure, the magnetic anisotropy of the Josephson current is a singular peculiarity for the RSOC experimentally. As presented above, when the exchange field $\vec{h}$ lies in different planes, there exist different features. As

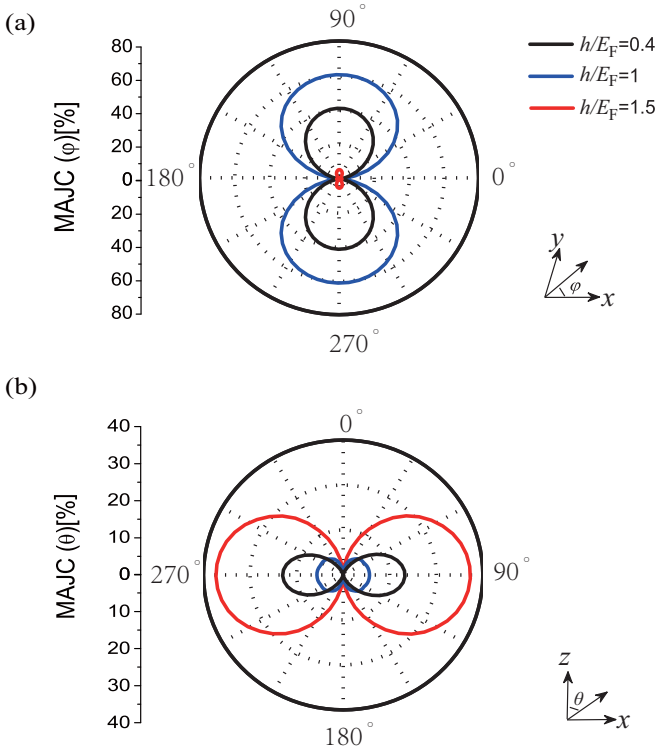

FIG. 8. (a) The in-plane MAJC as a function of φ and (b) out-of-plane MAJC as a function of θ for different h. The other parameters are unchanged.

usual, two configurations important for investigating transport anisotropies in vertical junctions are considered here. One is the "out of plane" with $\vec{h}$ in a plane perpendicular to the F layer, where the corresponding out-of-plane MAJC is defined as

$$MAJC(\theta) = \left.\frac{I_c(0,\varphi) - I_c(\theta,\varphi)}{I_c(\theta,\varphi)}\right|_{\varphi=-90^\circ}.$$

The other is the "in plane" with $\vec{h}$ in a plane parallel to the F layer, whose MAJC is given by

$$MAJC(\varphi) = \left.\frac{I_c(\theta,0) - I_c(\theta,\varphi)}{I_c(\theta,\varphi)}\right|_{\theta=90^\circ}.$$

The angular dependences of the in-plane and out-of-plane MAJCs for different h in the present hybrid structure are shown in Fig. 8. Both the MAJCs are found to display nonmonotonic variations with h. For the in-plane configuration, the MAJC first increases with the enhancement of h and reaches its maximum at $h/E_F = 1$, with the F region being completely spin polarized, and then is highly suppressed for $h > E_F$, for instance, the MAJC is even approximately zero at $h/E_F = 1.5$. However, for the out-of-plane configuration, the MAJC is first increased with the enhancement of h and gets its maximum at $h/E_F = 0.4$, then decreases and reaches the minimum at $h/E_F = 1$, and finally increases all the time, which is thoroughly different from that for the in-plane configuration. Since the MAJC essentially measures the current's "magnetosensitivity," especially "large" MAJC amplitudes should occur when tuning the junction through the transition point by changing magnetization orientations. Indeed, for $h/E_F = 0.4$ and 1.5, there exist rather pronounced MAJCs, which facilitates θ-controlled 0-π transitions [see Fig. 6(a)]. Furthermore, at the two exchange splittings, besides the rather pronounced MAJCs, the curve shapes for the MAJC with θ in Fig. 8(b) seem to be alike, while the MAJCs are relatively small in stable 0 states at $h/E_F = 1.0$, explaining the overall nonmonotonic h variations.

To have a high insight into the impact of RSOC on the magnitudes of MAJCs with or without the magnetically controlled 0-π transitions, we plot the angular dependencies of the in-plane and out-of-plane MAJCs for different RSOCs λ as shown in Fig. 9. The out-of-plane and in-plane MAJCs are found to be very sensitive to the change of the RSOC and vary monotonically with λ, which is contrary to that in the previous works. Furthermore, the previous studies showed that the in-plane anisotropy stems from the interplay of the interfacial Rashba and Dresselhaus spin-orbit fields [21–23], in other words, if either of the two fields is absent, the in-plane MAJC vanishes. The so-called interfacial spin-orbit coupling is due to the fact that in hybrid structures, two sides of the junction have different crystal and electronic structures, and the interface potential barrier is asymmetric, resulting in the Rashba and Dresselhaus type of SOC localized near the interface. The Rashba (or Bychkov-Rashba) field is present due to the space inversion asymmetry of the heterostructure. If bulk inversion symmetry is also broken, there will additionally be a spin-orbit field of the Dresselhaus type. In the F/S junctions with interfacial SOC, incoming electrons feel an effective wave vector **k**-dependent magnetic field which couples to their spin. And the in-plane anisotropy arises from the interference between the Rashba and Dresselhaus fields, which results in a C_{2v} symmetric field in the corresponding interface. It is worth noting that in the present structure, however, the in-plane MAJC is always exhibited in the absence of Dresselhaus spin-orbit field [see Figs. 9(a) and 9(c)].

The physics on the finite in-plane MAJC in the present structure can be described as follows, which is significantly different from that for the interfacial SOC [19,22]. Due to the RSOC, for the low-energy bands with the Dirac-like dispersion in graphene, there exist the anisotropic spin splitting of band around the K (K') point [47]. One spin subband undergoes trigonal-warping deformation, while the opposite-spin subband is still almost of isoenergy with spin precession. The RSOC-induced spin splitting can be considered to correspond to an effective exchange field. Its direction is closely connected with the wave vector direction and its magnitude is also anisotropic. Therefore, for a fixed in-plane magnetization of the F region, its exchange field and the effective one of the RSOC region are almost always noncollinear. This means that the spin-triplet AR is induced as in an F/F/S junction with the noncollinear magnetic configuration [48], which in fact corresponds to the k-independent spin flip due to the RSOC. In the F/F/S junction, the spin-triplet AR probability amplitude is determined by the angle between the exchange field directions of the two Fs. Therefore the corresponding spin-triplet AR probability amplitude in the present structure is strongly dependent on the magnetization orientation of the F. In other words, the AR including the specular AR is magnetoanisotropic and thus the in-plane MAJC always

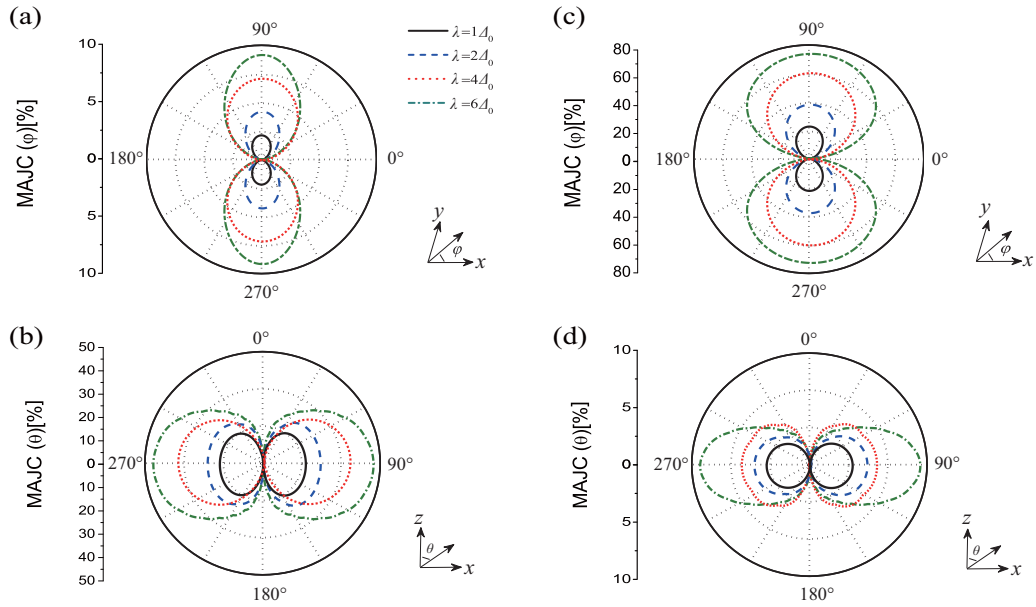

FIG. 9. The in-plane MAJC as a function of φ for $h/E_F = 1.5$ (a) and 1 (c), and the out-of-plane MAJC as a function of θ for the same h (b) and (d) as in (a) and (c), respectively. Here, various λ are marked in the figure and the other parameters are unchanged.

remains finite. In the AR process, the incident electron and Andreev-reflected hole come from different valleys, and their chiralities for the retro-AR are the same while opposite for the specular one.

It is worth mentioning that in the unphysical coordinate system with the x axis not being along the Josephson current direction, the finite in-plane MAJC can be also exhibited. This is because the exchange field direction of the F and the effective one of the RSOC region are still almost always noncollinear. With the magnetization direction of the F varying, the angle between the two exchange field directions is also changed, and thus there still exists the AR's magnetoanisotropy.

The explanation of the finite in-plane MAJC in graphene-based Josephson junctions only in presence of RSOC can be also given by the ABS magnetoanisotropies. The ABSs, carrying the Josephson currents, are also shown to be magnetoanisotropic with φ, which are not presented by figures for simplicity here. This indicates that the Josephson current is magnetoanisotropic as well; therefore, the resultant in-plane MAJC can be finite.

The curve shapes, ellipses for the in-plane MAJCs with φ at different λ, appear to be all similar, and the ellipses are enlarged with the increase of λ, as shown in Figs. 9(a) and 9(c), which means that for a fixed φ, the in-plane MAJC monotonically varies with λ. These modulations also suggest no λ-induced 0-π transitions.

The great increase of out-of plane MAJC amplitudes at $h/E_F = 1.5$ is shown with λ in Fig. 9(b). At about $\pi/4$ of θ [see Fig. 6(a), the point of 0-π transition at $h/E_F = 1.5$], the MAJC $\approx$25% for $\lambda = 4\Delta_0$, while it is $\approx$40% for $\lambda = 6\Delta_0$. Since the RSOC does not induce the 0-π transition, the enhancement of λ is in favour of identifying the vicinity of a 0-π transition from MAJC measurements. However, for parameters far away from magnetically controlled 0-π transitions, e.g., $h/E_F = 1$, the junctions are in stable 0 states and the MAJCs are obviously smaller as compared with $h/E_F = 1.5$ [see Fig. 9(d)]. For the in-plane MAJC, the situation is just contrary. The in-plane MAJC can reach 80% at $h/E_F = 1$ [see Fig. 9(c)], while its maximum is not beyond 9% at $h/E_F = 1.5$ [see Fig. 9(a)].

The magnetoanisotropic features of Figs. 8 and 9 can be all ascribed to the interplay of the proximity-induced RSOC and ferromagnetism in graphene combined with chiral nature of the carriers, which can be seen from the above explanation of the finite in-plane MAJC. Specifically, the combination of the ferromagnetism with the chiral nature of the quasiparticles, Dirac-like linear dispersion, and **k**-independent spin-flip mechanism in the graphene interlayer leads to the highly magnetoanisotropic equal-spin triplet AR including the specular one. And thus the resultant quantum tunneling transport in the present heterojunction becomes highly magnetoanisotropic, which is qualitatively different from the case for normal, nonrelativistic electrons. Here, for a ferromagnetic graphene sheet with the Dirac-like linear dispersion at low energies, the normal Fermi level at Dirac point ($E_F = 0$) is shifted by the exchange field, which is characterized by the specular AR in the ferromagnetic graphene-based S hybrid structure. In the presence of the RSOC, the equal-spin triplet AR, particularly, the specular one at $h > E_F$, is induced. The chiral nature of the carriers in graphene is formally a projection of pseudospin on the direction of motion, which is positive and negative for electrons and holes, respectively.

IV. CONCLUSIONS

We have shown that the graphene-based S/F/R/S Josephson junctions display a very rich and experimentally accessible magnetoanisotropic Josephson effect induced by the RSOC, which is characteristic by the triplet equal-spin pairs. Two kinds of 0-π transitions, the two significant experimental signatures for the structure, are exhibited. One is that in the

presence of the RSOC, one 0-π transition is observed by manipulating the orientation of exchange field $\vec{h}$. It is strongly dependent on the magnitude of $\vec{h}$ that must be periodically taken from nE_F to $(n+1/2)E_F$ with $n = 0, 1, 2, \ldots$, where the θ corresponding to the transition point can be from 0.25π to 0.35π. The other is that tuning the magnitude of $\vec{h}$ allows for the periodical appearance of a 0-π transition in a considerable scope of the orientation ($\theta = 0 \sim \pi/3$). In addition, there exist two different types of anomalous Josephson current effect by controlling the orientation of $\vec{h}$: one corresponds to either the positive or negative Josephson current at zero phase shift, the other corresponds only to the negative. Specifically, the in- and out-of-plane MAJCs are found to vary monotonically with λ while nonmonotonically with h, which are observable experimental characteristics for the present hybrid structure. For the former the in- and out-of-plane MAJCs can reach 15% and 35%, respectively, while for the latter they reach 17% and 60%, respectively. It is pointed out here that for an observable finite magnitude of MAJC, $\lambda \geqslant 4$ meV and $h \geqslant 10$ meV are needed, which can be experimentally achieved.

These obtained characteristics, being particular to such hybrid junctions due to the Dirac-like band structure, may confirm the proximity-induced RSOC in the graphene. State-of-the-art experimental techniques have recently made it possible to quantitatively measure the current-phase relation of the ballistic graphene Josephson junctions by a fully gate-tunable graphene superconducting quantum interference device [49]. With recent experimental advances, we hope that this work will stimulate future experiments involving graphene-based magnetoanisotropic Josephson devices.

ACKNOWLEDGMENT

This work was supported by the National Natural Science Foundation of China under Grants No. 11874221, No. 11574045, and No. 11704190, and the Natural Science Foundation of Jiangsu Province under Grant No. BK20171030.

[1] H. B. Heersche, P. J. Herrero, J. B. Oostinga, L. M. K. Vandersypen, and A. F. Morpurgo, Nature (London) **446**, 56 (2007).
[2] P. Jarillo-Herrero, J. A. van Dam, and L. P. Kouwenhoven, Nature (London) **439**, 953 (2006).
[3] D. Perconte, F. A. Cuellar, C. Moreau-Luchaire, M. Piquemal-Banci, R. Galceran, P. R. Kidambi, Marie-Blandine Martin, S. Hofmann, R. Bernard, B. Dlubak, P. Seneor, and J. E. Villegas, Nat. Phys. **14**, 25 (2018).
[4] A. Di Bernard, O. Millo, M. Barbone, H. Alpern, Y. Kalcheim, U. Sassi, A. K. Ott, D. De Fazio, D. Yoon, M. Amado, A. C. Ferrari, J. Linder, and J. W. A. Robinson, Nat. Commun. **8**, 14024 (2017).
[5] P. Wei, S. Lee, F. Lemaitre, L. Pinel, D. Cutaia, W. Cha, F. Katmis, Y. Zhu, D. Heiman, J. Hone, J. S. Moodera, and C. T. Chen, Nat. Mater. **15**, 711 (2016).
[6] J. C. Leutenantsmeyer, A. A. Kaverzin, M. Wojtaszek, and B. J. van Wees, 2D Mater. **4**, 014001 (2017).
[7] B. Karpiak, A. Dankert, A. W. Cummings, S. R. Power, S. Roche, and S. P. Dash, 2D Mater. **5**, 014001 (2018).
[8] J. S. Xu, S. Singh, J. Katoch, G. Wu, T. Zhu, L. Žutić, and R. K. Kawakami, Nat. Commun. **9**, 2869 (2018).
[9] Z. Y. Wang, C. Tang, R. Sachs, Y. Barlas, and J. Shi, Phys. Rev. Lett. **114**, 016603 (2015).
[10] M. Zareyan, H. Mohammadpour, and A. G. Moghaddam, Phys. Rev. B **78**, 193406 (2008).
[11] A. G. Moghaddam and M. Zareyan, Phys. Rev. B. **78**, 115413 (2008).
[12] I. Žutić, J. Fabian, and S. Das Sarma, Rev. Mod. Phys. **76**, 323 (2004).
[13] J. Fabian, A. Matos-Abiague, C. Ertler, P. Stano, and I. Žutić, Acta Phys. Slovaca **57**, 565 (2007).
[14] A. Avsar, J. Y. Tan, T. Taychatanapat, J. Balakrishnan, G. K. W. Koon, Y. Yeo, J. Lahiri, A. Carvalho, A. S. Rodin, E. C. T. O'Farrell, G. Eda, A. H. Castro Neto, and B. Özyilmaz, Nat. Commun. **5**, 4875 (2014).
[15] T. Yokoyama, Y. Tanaka, and J. Inoue, Phys. Rev. B **74**, 035318 (2006).
[16] X. Zhai and G. Jin, Phys. Rev. B **89**, 085430 (2014).
[17] Y. Yang, C. Bai, X. Xu, and Y. Jiang, Carbon **122**, 150 (2017).
[18] C. S. Huang, Y. Yang, Y. C. Tao, and J. Wang, New J. Phys. **22**, 033018 (2020).
[19] J. Linder and T. Yokoyama, Phys. Rev. Lett. **106**, 237201 (2011).
[20] P. Lv, Y.-F. Zhou, N.-X. Yang, and Q.-F. Sun, Phys. Rev. B **97**, 144501 (2018).
[21] Q. Qiang and Q.-F. Sun, Phys. Rev. B **99**, 184507 (2019).
[22] P. Högl, A. Matos-Abiague, I. Žutić, and J. Fabian, Phys. Rev. Lett. **115**, 116601 (2015).
[23] A. Costa, P. Högl, and J. Fabian, Phys. Rev. B **95**, 024514 (2017).
[24] D. B. Szombati, S. Nadj-Perge, D. Car, S. R. Plissard, E. P. A. M. Bakkers, and L. P. Kouwenhoven, Nat. Phys. **12**, 568 (2016).
[25] M. Minutillo, D. Giuliano, P. Lucignano, A. Tagliacozzo, and G. Campagnano, Phys. Rev. B **98**, 144510 (2018).
[26] R. Beiranvand, H. Hamzehpour, and M. Alidoust, Phys. Rev. B **94**, 125415 (2016).
[27] A. Furusaki and M. Tsukada, Solid State Commun. **78**, 299 (1991).
[28] G. E. Blonder, M. Tinkham, and T. M. Klapwijk, Phys. Rev. B **25**, 4515 (1982).
[29] C. W. J. Beenakker, Phys. Rev. Lett. **97**, 067007 (2006).
[30] C. W. J. Beenakker, Rev. Mod. Phys. **80**, 1337 (2008).
[31] M. B. Shalom, M. J. Zhu, V. I. Fal'ko, A. Mishchenko, A. V. Kretinin, K. S. Novoselov, C. R. Woods, K. Watanabe, T. Taniguchi, A. K. Geim, and J. R. Prance, Nat. Phys. **12**, 318 (2016).
[32] M. Gmitra, S. Konschuh, C. Ertler, C. Ambrosch-Draxl, and J. Fabian, Phys. Rev. B **80**, 235431 (2009).
[33] S. Abdelouahed, A. Ernst, K. J Hen., I. V. Maznichenko, and I. Mertig, Phys. Rev. B **82**, 125424 (2010).
[34] Y. F. Hsu and G. Y. Guo, Phys. Rev. B **81**, 045412 (2010).
[35] C. W. J. Beenakker, Phys. Rev. Lett. **67**, 3836 (1991).
[36] A. A. Golubov, M. Yu. Kupriyanov, and E. Ilichev, Rev. Mod. Phys. **76**, 411 (2004).

[37] M. Chtchelkatchev, W. Belzig, Yu. V. Nazarov, and C. Bruder, JETP Lett. **74**, 323 (2001).
[38] M. J. M. de Jong and C. W. J. Beenakker, Phys. Rev. Lett. **74**, 1657 (1995).
[39] V. V. Ryazanov, V. A. Oboznov, A. Yu. Rusanov, A. V. Veretennikov, A. A. Golubov, and J. Aarts, Phys. Rev. Lett. **86**, 2427 (2001).
[40] A. Sakurai, Progr. Theor. Exp. Phys. **44**, 1472 (1970).
[41] G. Annunziata, H. Enoksen, J. Linder, M. Cuoco, C. Noce, and A. Sudbo, Phys. Rev. B **83**, 144520 (2011).
[42] C. W. J. Beenakker and H. van Houten, Phys. Rev. Lett. **66**, 3056 (1991).
[43] H. Zhang, J. Wang, and J. F. Liu, Appl. Phys. Lett. **108**, 102601 (2016).
[44] I. V. Krive, A. M. Kadigrobov, R. I. Shekhter, and M. Jonson, Phys. Rev. B **71**, 214516 (2005).
[45] O. V. Dimitrova and M. V. Feigel'man, J. Exp. Theor. Phys. **102**, 652 (2006).
[46] L. Dell'Anna, A. Zazunov, R. Egger, and T. Martin, Phys. Rev. B **75**, 085305 (2007).
[47] P. Rakyta, A. Kormányos, and J. Cserti, Phys. Rev. B **82**, 113405 (2010).
[48] Z. Ping Niu and D. Y. Xing, Phys. Rev. Lett. **98**, 057005 (2007).
[49] G. Nanda, J. L. A. Servin, P. Rakyta, A. Kormányos, R. Kleiner, D. Koelle, K. Watanabe, T. Taniguchi, L. M. K. Vandersypen, and S. Goswami, Nano Lett. **17**, 3396 (2017).